A Comprehensive Multi-Functional Controller for Hybrid Energy Storage Systems in DC Microgrids

Xin Lin, *Student Member*, *IEEE*, Ramon Zamora, *Senior Member*, *IEEE*, and Craig A. Baguley, *Member*, *IEEE*

***Abstract*—This article proposes a comprehensive multi-functional controller for a hybrid energy storage system (HESS), including a battery and supercapacitor (SC). In the presented method, a *V*-d*P*/dt is proposed to control the output power of the battery converter with a slow dynamic response. The traditional *V*-*P* droop is employed to regulate the SC converter to give a fast response. The dc bus voltage can be maintained in a safe range by the SC converter control so that no voltage recovery loop is required. Hence, the order of the overall control system and the complexity of parameter design can be reduced. In addition, a novel consensus-based voltage compensator is proposed to achieve the state of charge (SoC) balance and accurate power sharing among batteries. Then, an SoC restoration of the SC is used to address the leakage current and ensure sufficient energy for future use. Next, a power management scheme (PMS) is proposed to protect the batteries from over-use under different operating modes. Finally, the output impedance characteristics, control system design, and stability analysis are elaborated. The processor in the loop (PIL) simulation results verified the effectiveness and feasibility of the proposed control method.**

***Index Terms*—Consensus algorithm, DC microgrid, droop control, hybrid energy storage system, power management, state of charge balance.**

NOMENCLATURE

CVC	Constant voltage control
ESS	Energy storage system
HESS	Hybrid energy storage system
MPPT	Maximum power point tracking
PMS	Power management system
PV	Photovoltaic
SC	Supercapacitor
SoC	State of charge
a_{jl}	Connection status
$h_j(\cdot)$	Information status for j^{th} agent
i, i_o	Output and initial current of the inductor
$k^p_{\text{sc},j}$, $k^i_{\text{sc},j}$	Control parameters for SC recovery
$k^p_{\text{SoC},j}$, $k^i_{\text{SoC},j}$	Control parameters for SoC recovery
$k^p_{\text{acc.},j}$, $k^i_{\text{acc.},j}$	Control parameters for accurate power sharing
k_x^{cp}, k_x^{ci}	Control parameters for current loop
k_x^{vp}, k_x^{vi}	Control parameters for voltage loop
L	Inductance
L_x, C_x	Filter inductor and capacitor
m, n	Droop coefficients
$P_{b,j}$, $P_{\text{sc},j}$	Output power of the j^{th} battery and SC
$P_{t,j}$	Total output power of HESS
$P^{\text{p.u.}}_{r,j}(k{+}1)$	The reference power in per unit
P_{pv}	PV power
P_g	Grid power
P_{load}	Load power
P_{loss}	Power loss
R^L_b, R^L_{sc}	Line resistances
s	Laplace operator
$\text{SoC}^r_{b,j}(k{+}1)$	Reference SoC of the j^{th} battery
$\text{SoC}^m_{b,j}$	Measured SoC of the j^{th} battery
v_L, v_o	Output and initial voltage of inductor
v_r	Reference voltage
$v_{b,j}$, $v_{\text{sc},j}$	Output voltage of the j^{th} battery and SC
$v^r_{\text{sc},j}$, $v^{\text{in}}_{\text{sc},j}$	Reference and measured input voltage of the SC
ε	Convergence speed
$\delta_{jl}(\cdot)$	Cumulative difference between agents j and l
τ	Communication delay
$\omega_{x,v}$, $\omega_{x,c}$	Double loop control bandwidth

Authors are with the Electrical and Electronic Engineering Department, Auckland University of Technology, 1142 Auckland, New Zealand, e-mails: (xin.lin@aut.ac.nz, ramon.zamora@aut.ac.nz, and craig.baguley@aut.ac.nz).

I. INTRODUCTION

NOWADAYS, dc microgrid is receiving more attention due to the increasing penetration of dc power sources, such as photovoltaic (PV) sources. Energy storage systems (ESSs) are an integral part of a dc microgrid that can suppress power fluctuations caused by the mismatch between power generation and demand [1], [2]. ESSs can be implemented using a variety of energy storage types, with each type having distinct characteristics that enable the realization of specific benefits [3]. For example, batteries with a slow dynamic response and a high energy density, may be employed to supply load power in steady state [4]. Conversely, supercapacitors (SCs), with a fast dynamic response but a low energy density, may be employed to serve loads with high power fluctuations [5]. No existing

energy storage type has characteristics that suit all load and user demands. Therefore, hybrid energy storage systems (HESS), comprising multiple energy storage types have been proposed as an effective solution [6].

Many published works have presented various control methods for HESS research [7]-[11]. In [7], a frequency-coordinating virtual impedance control scheme is proposed to accomplish transient power allocations in HESS. However, the method fails to consider the bus voltage deviations. In [9], a novel energy management system is proposed for the grid-connected HESS under different operating modes. With the proposed method, the power sharing between battery and SC can be effectively achieved. Besides, the output power of the battery in HESS is based on the SoC level. Therefore, the over-use of the battery can be avoided. However, the methods mentioned above only use a single HESS to suppress the power fluctuations. As a result, the load pressure of the HESS will be increased, thereby reducing the service life of the ESS components.

To solve these shortcomings, control methods for multiple HESSs have also been studies in [12]-[18]. A novel droop control in [12] is proposed to achieve different dynamic power-sharing for multiple HESSs. By using this method, a conventional *V*-*P* droop control is used to regulate the battery converter to deliver the lower-frequency power, while an integral droop control is used to regulate the SC converter to supply the higher-frequency power. However, the proposed method does not consider the issue of the bus voltage deviation. In [13], a decentralized power management scheme (PMS) for HESSs is proposed to realize the power-split, voltage recovery and SoC of SC restoration. However, the order of overall control system is higher. In [15], an advanced secondary voltage recovery control is proposed for a battery and SC system in dc microgrid. In presented method, a voltage restoration based on consensus algorithm is used to maintain the dc bus voltage within the acceptable range. Another voltage recovery control is used to restore the SoC of the SC to pre-set value. In [16] and [17], a semi-consensus strategy is designed to implement the power sharing, SoC balance among batteries, and SoC restoration of SCs. Within the semi-consensus scheme, only the local controllers for batteries exchange data through a sparse communication link. However, the controllers for SCs do not need to carry out the data exchange process, thus saving the system investment cost.

Although the above-mentioned articles have studied HESS in the DC microgrid, their shortcomings can be summarized as follows:

- Refs. [12]-[17] adopt power/current based droop control to realize the power distribution between batteries and SCs, which causes a steady-state voltage deviation in the DC bus voltage. Therefore, these methods require additional voltage recovery control to ensure that the DC bus voltage is at the set value. Additional voltage recovery system will increase the order of the overall control system and the design complexity of control parameters.
- Refs. [16]-[17] are able to achieve SoC balancing among batteries under a single DC bus condition. However, different line resistances can reduce the average power sharing among batteries, resulting in poor performance of SoC balancing schemes. In addition, the methods in [12]-[16] may lead to over-charging and -discharging of the battery.
- The methods in refs. [7] – [11] are proposed for single HESS. For multiple HESSs, these methods may require redesign of control parameters, thus they may not be suitable for multiple HESSs under multiple DC bus systems.
- In addition, the control structure in [18] includes derivative term that amplifies the noise of the system, thereby reducing the stability of the system. Besides, the accuracy of the SoC balance is poor due to different line resistances among DC buses.

To solve these drawbacks, a comprehensive multi-functional controller for HESSs in dc microgrid is proposed in this article. The major contributions of this article can be summarized as follows:

a) A droop-based coordinated control is proposed to realize power sharing between battery and SC, and regulate DC bus voltage without additional voltage restoration control. Therefore, the order of the control system and the complexity of parameter design are reduced. By adopting the proposed method, a *V*-d*P*/dt control is proposed to regulate the battery converter to provide average power, while the traditional *V*-*P* droop method is employed to adjust the SC converter to supply transient power. The bus voltage is regulated by the SC converter.
b) A novel consensus-based voltage compensator including SoC balancing and accurate power sharing schemes is proposed to eliminate the SoC imbalance among batteries and the adverse influence of the different line resistances in the multiple DC bus systems.
c) The PMS is proposed to protect batteries from over-charging and -discharging under different operating modes, including islanded, grid-connected, and plug-and-play (PnP) modes. The voltage compensation control of the SC is employed to solve the leakage current and to guarantee sufficient energy for continuous operation.
d) The impedance characteristics of the proposed strategy are analyzed in the frequency domain, and the root locus method is adopted to show system stability.

The rest of this paper is organized as follows. Section II presents the local control methods. Section III describes the consensus-based power compensator. In Section IV, the PMS is proposed for HESS. The parameter design and stability analysis of the proposed control methods are explained in detail in Section V. Section VI presents simulation results and discussions. The conclusions are presented in Section VII.

II. Proposed Local Control Methods

A. System Description

Fig. 1. Depicts a dc microgrid, which consists of renewable energy sources (RESs) such as PVs, multiple HESSs, and loads. PVs operate in maximum power point tracking (MPPT) and

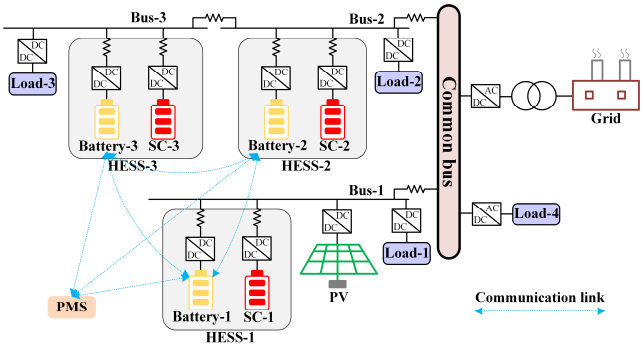

Fig. 1. The configuration of dc microgrid with the integration of HESSs.

constant voltage control (CVC) modes. HESSs can suppress power fluctuations and maintain bus voltages. The PMS can ensure the SoC of the batteries within a safe horizon, thereby preventing batteries overuse.

B. *V*-d*P*/dt *and V-P Droop Controls*

The *V*-d*P*/dt control is discovered from the inductor characteristic, which appears as a short circuit at low frequency and as an open circuit at high frequency. Therefore, the battery converter can be controlled to provide low dynamic power instead of transient power at steady state. Based on the inductor characteristic, the relationship between inductor current and voltage can be written as (1).

$$i = i_o - \frac{1}{L}\int v_L dt \tag{1}$$

where L, i_o, i, and v_L are inductance, inductor initial current, the output current and voltage of the inductor, respectively. Then, (1) can be further modified as (2).

$$v_L = v_o - L\frac{di}{dt} \tag{2}$$

where $v_o = Ldi_o/dt$. Performing Laplace transform, equation (2) can be further written as (3).

$$v_L = v_o - sLi \tag{3}$$

where s is the Laplace operator. Assuming s = $j\omega$, equation (3) can be modified as (4).

$$v_L = v_o - j\omega Li \tag{4}$$

where ω and j are angular frequency and imaginary unit. From the second term ($j\omega Li$) of (4), when the angular frequency decreases, the inductive reactance also becomes lower, and vice versa. Therefore, from the perspective of frequency domain, the second term of (4) can be regarded as an LPF, which filters out the high frequency power/current. In addition, the second term (Ldi/dt) in (2) is defined as a voltage drop. The format of (2) is then very similar to conventional current-based droop control. Furthermore, the equivalent mathematical model of droop control is to subtract a voltage drop from the set voltage to obtain an output voltage that will be used as a reference voltage for dual-loop control. Therefore, equation (2) can also be considered as a kind of droop control equation. Finally, similar to (2), the *V*-d*P*/dt control shown in (5) is designed by replacing current with power and retaining the equivalent format as (2).

$$v_{b,j} = v_r - m\frac{dP_{b,j}}{dt} \tag{5}$$

where v_r, m, $v_{b,j}$, and $P_{b,j}$ are the reference voltage, droop coefficient, output voltage and power of the j^{th} battery converter, (j = 1, 2, …, N). The method in (5) contains a derivative term that amplifies system noise in the frequency domain. Therefore, (5) is further modified to (6).

$$P_{b,j} = \int \frac{v_r - v_{b,j}}{m} dt. \tag{6}$$

From (6), the derivative term has been eliminated. Besides, the ratio of output power to input voltage will be delivered to the current controller as the reference current. Therefore, the battery controller does not require a voltage controller, thereby simplifying the complexity of the control system.

The *V-P* droop control of the SC can be represented by (7) based on [19].

$$v_{\text{sc},j} = v_r - nP_{\text{sc},j} \tag{7}$$

where $v_{\text{sc},j}$ and $P_{\text{sc},j}$ are the output voltage and power of the j^{th} SC converter terminal, respectively. n is the droop coefficient that can be calculated by (8).

$$n = \frac{v_{\max} - v_{\min}}{P_{\text{sc},j}^{\max}} \tag{8}$$

where $v_{\min}$ and $v_{\max}$ are the minimum and maximum allowable dc bus voltage; $P_{\text{sc},j}^{\max}$ is the maximum transient power of the SC converter. Since the battery and SC can simultaneously meet the different dynamic power demands of the system, the total output power $P_{t,j}$ of HESS is the sum of the $P_{b,j}$ and $P_{\text{sc},j}$, as given in (9).

$$P_{t,j} = P_{b,j} + P_{\text{sc},j}. \tag{9}$$

If the voltage drops across converter line resistances are ignored, then the output voltages of the battery and SC converters are considered to be equal as shown by (10).

$$v_{b,j} = v_{\text{sc},j}. \tag{10}$$

By performing Laplace transform and combining (5), (7), (9) and (10), the power-split in the HESS can be written as (11).

$$\begin{cases} P_{b,j} = G_{\text{LPF}}(s)\cdot P_{t,j} = \dfrac{n}{ms+n}P_{t,j} \\ P_{\text{sc},j} = G_{\text{HPF}}(s)\cdot P_{t,j} = \dfrac{ms}{ms+n}P_{t,j}. \end{cases} \tag{11}$$

It can be seen from (11) that the essence of coordinated droop control is to form the low-pass filter (LPF) $G_{\text{LPF}}(s)$ and high-pass filter (HPF) $G_{\text{HPF}}(s)$ in HESS. Therefore, the output power of HESS can be automatically divided into low- and high-frequency parts, and then assigned each of them to the battery converter and SC converter, respectively. The desired power-sharing can be achieved by reasonably adjusting the corner frequency $\omega_c = n/m$ of both LPF and HPF.

C. *Voltage Recovery Method*

The characteristic of traditional *V-P* droop control is that power variations will cause bus voltage errors. In other words, if the power is constant, then the bus voltage will have steady-state voltage error. Since SC converter only provides transient power instead of continuous power, the bus voltage can be restored to the set value at steady state, no extra control is required. The principle of voltage restoration is summarized as follows:

- In the case of a sudden power change, the SC converter will immediately respond to suppress the power fluctuation of the system. Based on (7), the output voltage is expressed as (12).

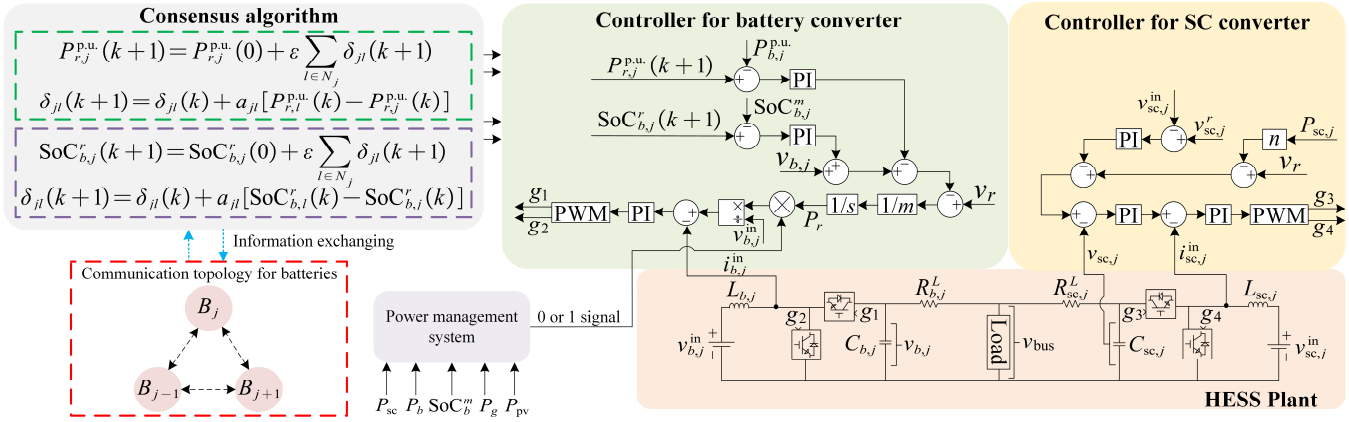

Fig. 2. The schematic diagram of the proposed control system for battery and SC converters.

$$v_{\min} \le v_{\mathrm{sc},j} = v_r - nP_{\mathrm{sc},j} \le v_{\max} \tag{12}$$

From (12), the output voltage caused by the SC converter releasing/absorbing transient power will be limited within the voltage minimum and maximum.

- After mitigating the power oscillation, the SC converter starts to slowly decrease its output power. When it reaches steady state, the SC converter no longer provides any output power to the system. Furthermore, the output power ($P_{\mathrm{sc},j}$) of the SC is equal to zero. Based on (12), the output voltage of the SC converter is equal to the reference bus voltage, as shown in (13).

$$v_{\min} \le v_{\mathrm{sc},j} = v_r \le v_{\max}. \tag{13}$$

- Finally, the bus voltage can be maintained within a safe range without the need for an additional voltage compensation loop.

D. Voltage Recovery Control for SCs

Due to the current leakage characteristics of the SC, the SoC of the SC will be reduced. To solve this problem, the *V-P* droop control with the SoC recovery is presented as (14).

$$v_{\mathrm{sc},j} = v_r - nP_{\mathrm{sc},j} - (k^p_{\mathrm{sc},j} + k^i_{\mathrm{sc},j}\frac{1}{s})(v^r_{\mathrm{sc},j} - v^{\mathrm{in}}_{\mathrm{sc},j}) \tag{14}$$

where $v^r_{\mathrm{sc},j}$ and $v^{\mathrm{in}}_{\mathrm{sc},j}$ are the reference and measured input voltage for the SC, respectively; $k^p_{\mathrm{sc},j}$ and $k^i_{\mathrm{sc},j}$ are the control parameters for the SC recovery method, respectively.

III. Consensus-Based Voltage Compensator

In HESS, the batteries are employed to provide continuous power at steady state. For batteries, the SoC imbalance is a significant issue, which results in the over-charging and -discharging of a certain battery. In addition, different line resistances can lead to inaccurate power among batteries, it may result in SoC balance not being successfully achieved. To address these issues, the consensus-based voltage compensator is proposed in this article.

A. Distributed Consensus Algorithm

A distributed consensus algorithm is an update rule that enables the status of distributed agents to be consistent by exchanging the information through sparse communication network [20]. In case of the HESSs, the distributed agents update their information status based on information gathered from neighbors. According to the information status of the distributed agents, the consensus algorithm generates a uniform value, which is sent as a control signal to the controllers of the distributed agents [21]. A distributed consensus algorithm is expressed as (15) – (16) based on [22].

$$h_j(k{+}1) = h_j(0) + \varepsilon \sum_{l\in N_j} \delta_{jl}(k{+}1) \tag{15}$$

$$\delta_{jl}(k{+}1) = \delta_{jl}(k) + a_{jl}\left[h_l(k) - h_j(k)\right] \tag{16}$$

where k is an iteration counter value. $h_j(k{+}1)$ is the information status of iteration at $k{+}1$ for j^{th} agent. N_j is the set of the agents that connect with j^{th} agent. $\delta_{jl}(k)$ is a variable, which can store cumulative difference between two agents j and l, and $\delta_{jl}(0) = 0$. a_{jl} is connection status between agents j and l. If agent j and agent l are not neighbors, then $a_{jl} = 0$, otherwise $a_{jl} = 1$. ε is used to regulate the convergence speed, which can be calculated by (17) based on [23].

$$\varepsilon = \frac{2}{\beta_1(L) + \beta_{n-1}(L)} \tag{17}$$

where $\beta_j(\cdot)$ is the j^{th} largest eigenvalue of the symmetric matrix. L is the Laplacian matrix; more detail can be found in [24].

B. Consensus-Based Voltage Compensator for Batteries

The consensus-based voltage compensator as defined by (18) – (19) is applied.

$$P_{b,j} = \int \frac{v_r - (v_{b,j} + \delta v_j)}{m} dt \tag{18}$$

$$\delta v_j = \delta v_{\mathrm{SoC},j} - \delta v_{\mathrm{acc.},j} \tag{19}$$

where δv_j is the voltage compensation term. $\delta v_{\mathrm{SoC},j}$ and $\delta v_{\mathrm{acc.},j}$ are used to adjust the setting voltage. $\delta v_{\mathrm{SoC},j}$ is the consensus-based SoC balancing control, which is written as (20) – (22).

$$\delta v_{\mathrm{SoC},j} = \left[\mathrm{SoC}^r_{b,j}(k{+}1) - \mathrm{SoC}^m_{b,j}\right](k^p_{\mathrm{SoC},j} + k^i_{\mathrm{SoC},j}\frac{1}{s}) \tag{20}$$

$$\mathrm{SoC}^r_{b,j}(k{+}1) = \mathrm{SoC}^r_{b,j}(0) + \varepsilon \sum_{l\in N_j} \delta_{jl}(k{+}1) \tag{21}$$

$$\delta_{jl}(k{+}1) = \delta_{jl}(k) + a_{jl}\left[\mathrm{SoC}^r_{b,l}(k) - \mathrm{SoC}^r_{b,j}(k)\right] \tag{22}$$

where $\mathrm{SoC}^r_{b,j}(k{+}1)$ and $\mathrm{SoC}^m_{b,j}$ are the reference and measured SoC of the j^{th} battery. $\mathrm{SoC}^r_{b,j}(0)$ is the initial SoC level. $k^p_{\mathrm{SoC},j}$ and $k^i_{\mathrm{SoC},j}$ are the proportional and integral parameters for the SoC balancing scheme.

The consensus-based accurate power control $\delta v_{\mathrm{acc.},j}$ is presented as (23) – (25).

$$\delta v_{\mathrm{acc.},j} = \left[P_{r,j}^{\mathrm{p.u.}}(k{+}1) - P_{b,j}^{\mathrm{p.u.}}\right]\left(k_{\mathrm{acc.},j}^{p} + k_{\mathrm{acc.},j}^{i}\frac{1}{s}\right) \tag{23}$$

$$P_{r,j}^{\mathrm{p.u.}}(k{+}1) = P_{r,j}^{\mathrm{p.u.}}(0) + \varepsilon \sum_{l\in N_j} \delta_{jl}(k{+}1) \tag{24}$$

$$\delta_{jl}(k{+}1) = \delta_{jl}(k) + a_{jl}\left[P_{r,l}^{\mathrm{p.u.}}(k) - P_{r,j}^{\mathrm{p.u.}}(k)\right] \tag{25}$$

where $P_{r,j}^{\mathrm{p.u.}}(k{+}1)$ is the reference power in per unit. It should be noted that the per unit power is the ratio of the reference power to the maximum power ($P_{\max}$) of the battery converter. $P_{r,j}^{\mathrm{p.u.}}(0)$ is the initial output power of the battery converter. $k_{\mathrm{acc.},j}^{p}$ and $k_{\mathrm{acc.},j}^{i}$ are the proportional and integral parameters for the accurate power controller, respectively. The control equivalent diagram is shown in Fig. 2. If the output power of the battery is less than the average power obtained by the consensus algorithm, the accurate power sharing control will generate a positive feedback voltage signal and send it to the droop control system to increase the reference voltage value, so that the output power of the battery will increase. On the contrary, if the battery power is greater than the average power, then the accurate power sharing method will send a negative feedback voltage signal to decrease the reference voltage of the control system, thereby reducing the output power of the battery. Therefore, accurate power sharing among batteries can be achieved. In addition, the proposed method requires a sparse communication system. Therefore, the transfer function of the communication delay can be expressed as (26).

$$G_d = \frac{1}{\tau s + 1} \tag{26}$$

where τ is the communication delay.

IV. Proposed PMS

The proposed PMS can ensure that the SoCs of the batteries are within a preset range. The equivalent circuit and flow chart of the proposed PMS is given in Figs. 2 and 3. It is worth noting that the SoC recovery loop of the SCs can ensure that the SoCs of the SCs are within a predetermined range. Therefore, PMS does not consider the SoC limitations of the SCs.

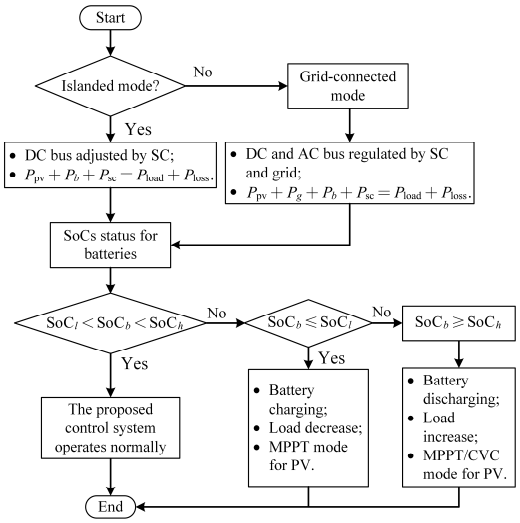

Fig. 3. The proposed PMS for HESSs.

In the islanded mode, the dc bus voltage is regulated by the SC converters. The system power balance can be expressed as (27).

$$P_{\mathrm{pv}} + P_b + P_{\mathrm{sc}} = P_{\mathrm{load}} + P_{\mathrm{loss}} \tag{27}$$

where P_{load} is the load power; P_{loss} is the power loss caused by the line impedance and the converters. The upper limit (SoC_h) and lower limit (SoC_l) can ensure the safe operation of the batteries.

Based on the SoC limits, the following three conditions are considered for the islanded mode:

1) $\mathrm{SoC}_l < \mathrm{SoC}_b < \mathrm{SoC}_h$: the HESS operates normally. The SCs supply the transient power, while the batteries provide the average power. The SoC imbalance among batteries is eliminated by the proposed consensus-based voltage compensator.
2) $\mathrm{SoC}_b \geq \mathrm{SoC}_h$: the batteries operate in discharging mode. If the power supplied by the PV and batteries is greater than the power demand, then the system will decrease the generated power. Besides, the PV controller will be switched from MPPT to CVC to reduce output power. It should be noted that this article focuses on the HESS control system rather than the PV system. Therefore, the control structure diagram of the PV system will not be given. However, ref. [25] can be referred for more detail information.
3) $\mathrm{SoC}_b \leq \mathrm{SoC}_l$: PV works in MPPT mode to provide maximum power to charge the batteries. In addition, the system load will be appropriately reduced.

In the grid-connected mode, the grid, PV, and HESSs simultaneously deliver power to the load. The dc and ac bus voltages are controlled by the SC converters and grid. The total power balance can be written as (28).

$$P_{\mathrm{pv}} + P_g + P_b + P_{\mathrm{sc}} = P_{\mathrm{load}} + P_{\mathrm{loss}} \tag{28}$$

where P_g is the grid power. The grid-connected mode also contains three conditions similar to the islanded mode to ensure that the SoCs of the batteries are within a safe range.

V. Control System Stability Analysis

In HESS, the SC converter uses dual-loop control, while the battery converter employs inner loop current control. The parameters of the control need to be well designed to ensure that the slow and fast dynamic power sharing can be achieved. The schematic diagram of the control circuit for battery and SC is drawn in Fig. 4. The control parameters can be found by using (29) based on [13], [18].

$$\begin{aligned} k_x^{\mathrm{cp}} &= \frac{\omega_{x,c} L_x}{v_r} \quad & k_x^{\mathrm{vp}} &= \frac{\omega_{x,v} C_x}{1-D} \\ k_x^{\mathrm{ci}} &= \frac{\eta \omega_{x,c}^2 L_x}{v_r} \quad & k_x^{\mathrm{vi}} &= \frac{\eta \omega_{x,v}^2 C_x}{1-D} \end{aligned} \tag{29}$$

where k_x^{cp}, k_x^{vp}, k_x^{ci}, and k_x^{vi} are the proportional and integral parameters for the current and voltage control, respectively. $\omega_{x,c}$ is the control bandwidth of the current loop. $\omega_{x,v}$ is the control bandwidth of the voltage loop. D denotes the steady state value of the duty cycle. η is a coefficient. r, L_x, and C_x are the resistance of inductor, filter inductor and filter capacitor of

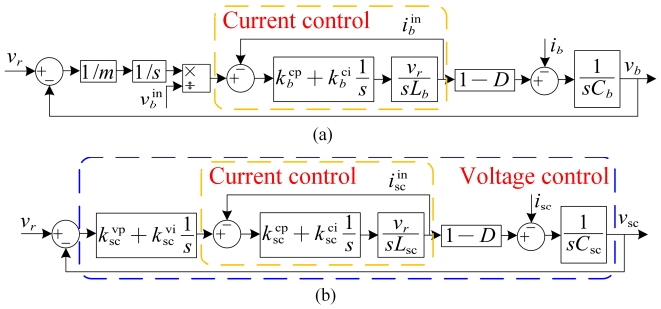

Fig. 4. The schematic diagram of the control circuit for dc-dc converter: (a) battery converter control, and (b) SC converter control.

the dc/dc converter, respectively. It should be noted that the response speed of the SC in HESS is faster than the response speed of the battery. Therefore, the current control bandwidth of the battery is smaller than the bandwidths of the SC. Specifically, $x = b$ denotes the battery, while $x = \mathrm{sc}$ denotes the SC component.

It is a common problem that the control system may suffer from potential degradation of stability caused by the coordination between interconnected converters [2]. Therefore, its stability analysis is an important step to ensure the safe operation of the system. According to Figs. 2 and 4, the small-signal model of the relationship between the bus voltage (v_{bus}) and the output voltage of the battery and SC converters is presented by (30).

$$\hat{v}_{\mathrm{bus}} = \frac{R_{\mathrm{sc}}^{L} R \hat{v}_b + R_b^{L} R \hat{v}_{\mathrm{sc}}}{R_{\mathrm{sc}}^{L} R + R_b^{L} R + R_b^{L} R_{\mathrm{sc}}^{L}} \tag{30}$$

where R_b^L and R_{sc}^L are the line resistance of the battery or SC. R is the load impedance. The small signal of the output volage of the battery converter can be obtained from (31).

$$\hat{v}_b = \frac{b_{13}s^3 + b_{12}s^2 + b_{11}s + b_{10}}{a_{15}s^5 + a_{14}s^4 + a_{13}s^3 + a_{12}s^2 + a_{11}s + a_{10}} \tag{31}$$

where $a_{15} = E_b(1-D)RP_{\max}C_b m v_b^{\mathrm{in}} L_b v_r$; $a_{14} = E_b R P_{\max}(1-D)C_b m v_b^{\mathrm{in}} \omega_{b,c} L_b + E_b P_{\max}(1-D) m v_b^{\mathrm{in}} L_b v_r$; $a_{13} = E_b(1-D)R P_{\max} C_b m v_b^{\mathrm{in}} \eta \omega_{b,c} L_b + E_b P_{\max}(1-D)^2 R \omega_{b,c} L_b + E_b P_{\max} m v_b^{\mathrm{in}} L_b (1-D)\omega_{b,c}$; $a_{12} = E_b P_{\max}(1-D)^2 R \eta \omega_{b,c}^2 L_b + P_{\max}(1-D) L_b \omega_{b,c} k_{\mathrm{SoC},j}^p + 2 v_b^{\mathrm{in}} E_b k_{\mathrm{acc.},j}^p + E_b(1-D) P_{\max} m v_b^{\mathrm{in}} \eta L_b v_r$; $a_{11} = L_b P_{\max}(1-D)\omega_{b,c} k_{\mathrm{SoC},j}^i + P_{\max}(1-D)\eta \omega_{b,c}^2 L_b k_{\mathrm{SoC},j}^p$; $a_{10} = P_{\max}(1-D)\eta \omega_{b,c}^2 L_b k_{\mathrm{SoC},j}^i + 2 v_b^{\mathrm{in}} E_b k_{\mathrm{acc.},j}^i$; $b_{13} = E_b(1-D)^2 R P_{\max} L_b \omega_{b,c} v_r$; $b_{12} = E_b(1-D)^2 R P_{\max} \eta \omega_{b,c}^2 v_r L_b$; $b_{11} = b_{10} = 0$.

Similarly, the small-signal model of the output voltage of the SC converter is given by (32).

$$\hat{v}_{\mathrm{sc}} = \frac{b_{23}s^3 + b_{22}s^2 + b_{21}s + b_{20}}{a_{24}s^4 + a_{23}s^3 + a_{22}s^2 + a_{21}s + a_{20}} \tag{32}$$

where $a_{24} = R E_{\mathrm{sc}}(1-D)C_{\mathrm{sc}}$; $a_{23} = R E_{\mathrm{sc}}(1-D)\omega_{\mathrm{sc},v} C_{\mathrm{sc}} + 2n\omega_{\mathrm{sc},v} C_{\mathrm{sc}} E_{\mathrm{sc}} v_{\mathrm{sc}}^{\mathrm{in}}$; $a_{22} = R E_{\mathrm{sc}}(1-D)\eta \omega_{\mathrm{sc},v}^2 C_{\mathrm{sc}} + \omega_{\mathrm{sc},v} C_{\mathrm{sc}} k_{\mathrm{sc},j}^p + 2n\eta \omega_{\mathrm{sc},v}^2 C_{\mathrm{sc}} E_{\mathrm{sc}} v_{\mathrm{sc}}^{\mathrm{in}} + E_{\mathrm{sc}}(1-D)$; $a_{21} = \omega_{\mathrm{sc},v} C_{\mathrm{sc}} k_{\mathrm{sc},j}^i + \eta \omega_{\mathrm{sc},v}^2 C_{\mathrm{sc}}$; $a_{20} = \eta \omega_{\mathrm{sc},v}^2 C_{\mathrm{sc}} k_{\mathrm{sc},j}^i$; $b_{23} = \omega_{\mathrm{sc},v} C_{\mathrm{sc}} R E_{\mathrm{sc}}(1-D)$; $b_{22} = \eta \omega_{\mathrm{sc},v}^2 C_{\mathrm{sc}} \times R E_{\mathrm{sc}}(1-D)$; $b_{21} = b_{20} = 0$.

Then, substituting (31) and (32) into (30), the characteristics function of the relationship between the bus voltage and the reference voltage is given as (33).

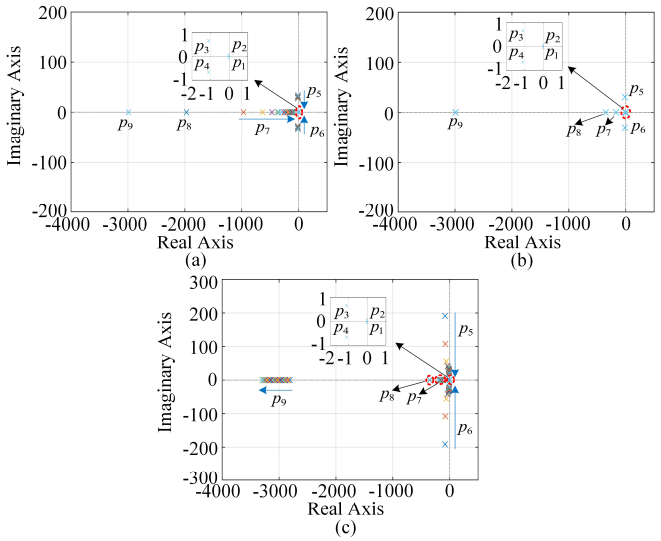

Fig. 5. Root locus diagrams: (a) C_b is between 10 μF and 200 μF, (b) C_{sc} is between 10 μF and 200 μF, and (c) n is between 0 and 0.01 V/W, while m is between 0 and 0.008 V/W.

$$0 = a_{39}s^9 + a_{38}s^8 + a_{37}s^7 + a_{36}s^6 + a_{35}s^5 + a_{34}s^4 + a_{33}s^3 + a_{32}s^2 + a_{31}s + a_{30} \tag{33}$$

where $a_{39} = a_{15}a_{24}$; $a_{38} = a_{15}a_{23} + a_{14}a_{24}$; $a_{37} = a_{15}a_{22} + a_{14}a_{23} + a_{13}a_{24}$; $a_{36} = a_{15}a_{21} + a_{14}a_{22} + a_{13}a_{23} + a_{12}a_{24}$; $a_{35} = a_{15}a_{20} + a_{14}a_{21} + a_{13}a_{22} + a_{12}a_{23} + a_{11}a_{24}$; $a_{34} = a_{14}a_{20} + a_{13}a_{21} + a_{12}a_{22} + a_{11}a_{23} + a_{10}a_{24}$; $a_{33} = a_{13}a_{20} + a_{12}a_{21} + a_{11}a_{22} + a_{10}a_{23}$; $a_{32} = a_{12}a_{20} + a_{11}a_{21} + a_{10}a_{22}$; $a_{31} = a_{11}a_{20} + a_{10}a_{21}$; $a_{30} = a_{10}a_{20}$.

According to equation (33), the system stability analysis can be achieved by observing the placement of the dominant pole in the root locus diagram. Then, selecting the appropriate parameters can ensure the performance of the controller and the safe operation of the system. From Fig. 5(a), there are nine negative eigenvalues, but only seven of them ($p_1, p_2, p_3, p_4, p_5, p_6$, and p_7) are dominant based on their position. With the variations of the filter capacitor C_b within the specified range, the dominant poles p_1, p_2, p_3, and p_4 are located in the left half of the s-plane. This indicates that the stability of the control system can be guaranteed. The poles p_5 and p_6 change from the complex conjugate poles to negative real poles. This indicates that the stability of the system is gradually improved. Meanwhile, although the dominant pole p_7 moves towards the right of the s-plane, it still sits on the left half of the s-plane. Therefore, the stability of the system can be guaranteed.

TABLE I
SYSTEM PARAMETERS

Items	Values	Items	Values	Items	Values
v_r	400 V	ω_c	0.2×2π rad/s	v_{sc}^r	180 V
v_b	180 V	m	0.0032 V/W	k_{SoC}^p	10
v_{sc}	200 V	n	0.004 V/W	k_{SoC}^i	1.1310
C_b	10 μF	k_b^{cp}	0.1257	$k_{\mathrm{acc.}}^p$	10
C_{sc}	10 μF	k_b^{ci}	157.9137	$k_{\mathrm{acc.}}^i$	0.6283
L_b	2 mH	$k_{\mathrm{sc}}^{\mathrm{cp}}$	0.0628	E_b	0.3 Ah
L_{sc}	5 mH	$k_{\mathrm{sc}}^{\mathrm{ci}}$	78.9568	$R_{b,1}^L, R_{\mathrm{sc},1}^L$	0.02 Ω
f_s	10 kHz	$k_{\mathrm{sc}}^{\mathrm{vp}}$	0.1257	$R_{b,2}^L, R_{\mathrm{sc},2}^L$	0.015 Ω
R	50 Ω	$k_{\mathrm{sc}}^{\mathrm{vi}}$	78.9568	$R_{b,3}^L, R_{\mathrm{sc},3}^L$	0.01 Ω
η	0.1	k_{sc}^p	2	$P_{\max}$	10 kW
ε	1/3	k_{sc}^i	0.1257	τ	1 ms

Similarly, Figs. 5(b) and 5(c) show that the dominant eigenvalues of the system are located on the left half of the s-plane by changing the specified parameters. Thus, the instability of the proposed control system can be eliminated.

VI. Simulation Verifications

To verify the effectiveness of the proposed method in real control system, the processor in the loop (PIL) platform including a microcontroller (MC) and PC, is established. The MC is implemented by using STM32F429ZIT6, connected in a closed loop with the controlled object. The microgrid configuration is shown in Fig. 1. The key parameters are listed in Table I.

A. Case 1: Different Dynamic Power-Sharing

In this case, the proposed method and the integral droop control from [12] are studied and compared. A single HESS including a battery and SC is used as the test object. From Fig. 6(a), HESS delivers 1 kW of power at the beginning. When the system load suddenly rises to 2 kW, the SC immediately responds to provide power and then gradually reduces to zero. The battery responds slowly to supply constant power at steady state. From Fig. 6(b), the dc bus voltage can be restored to the pre-set value through the SC control. According to the characteristics of *V-P* droop control, when SC provides the transient power, the dc bus voltage will have voltage deviations. After that, once the instantaneous power decreases to zero, the dc bus voltage will automatically return to the desired value. It can be seen from Fig. 6(c) that the simulation results produced by the control method from [12] are similar to the proposed method. However, when the system load changes, the dc bus voltage cannot be returned to the reference value, as shown in Fig. 6(d). This is because the dc bus voltage in [12] is regulated by the battery control (*V-P* droop control). This indicates that if the battery provides constant power, then the bus voltage error will always exist. Therefore, ref. [12] requires a voltage restoration loop to eliminate the steady state error of the bus voltage. The results show that the proposed method can realize dynamic power distribution and maintain the voltage at the set value without an additional control. Hence, it confirms that the presented approach outperforms the comparing method.

B. Case 2: The Performance of the Consensus-Based Voltage Compensator

As can be seen from Figs. 7(a) and 7(b), the methods in [17] and [18] cannot eliminate the SoC imbalance among batteries. The reason is that different line resistances among multiple DC bus leads to unequal power sharing, thereby degrading the performance of the SoC balancing strategy. From Figs. 7(c) and 7(d), although the error rate of the SoC balancing method in [18] is lower than that in [17], the SoC accuracy is still poor. From Fig. 7(e), the power sharing among batteries in [18] clearly presents the power deviations. From Fig. 7(f), the batteries cannot provide equivalent power to the load between 0-30 s. After 30 s, the consensus-based accurate power sharing control begins to operate, which can achieve a consistent output power from the batteries, thereby eliminating the negative effects of line resistance. It can be seen from Fig. 7(g) that the SoC of battery-1 (b_1) has the fastest drop rate, while the SoC of battery-3 (b_3) has the smallest drop rate. This means that the output power ($P_{b,1}$) of b_1 is the highest, while the output power ($P_{b,3}$) of b_3 is the least. Therefore, the SoC gap among batteries is gradually narrowing. In charging mode, the SoC of b_3 rises the fastest, and the SoC of b_1 rises the slowest. Therefore, SoC balance between batteries can be achieved, as shown in Fig. 7(h). Therefore, the proposed method performs significantly better than the methods in the previous conference article and [17].

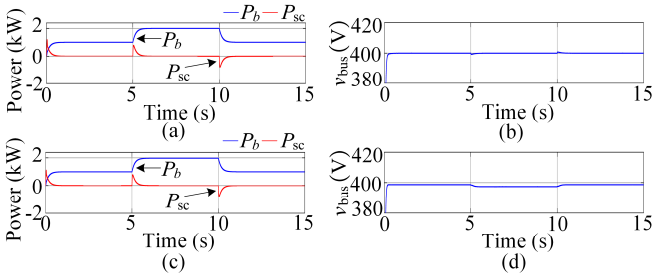

Fig. 6. Simulation results for case 1: (a) Dynamic power-sharing, (b) DC bus voltage, (c) Dynamic power-sharing from [12], and (d) DC bus voltage from [12].

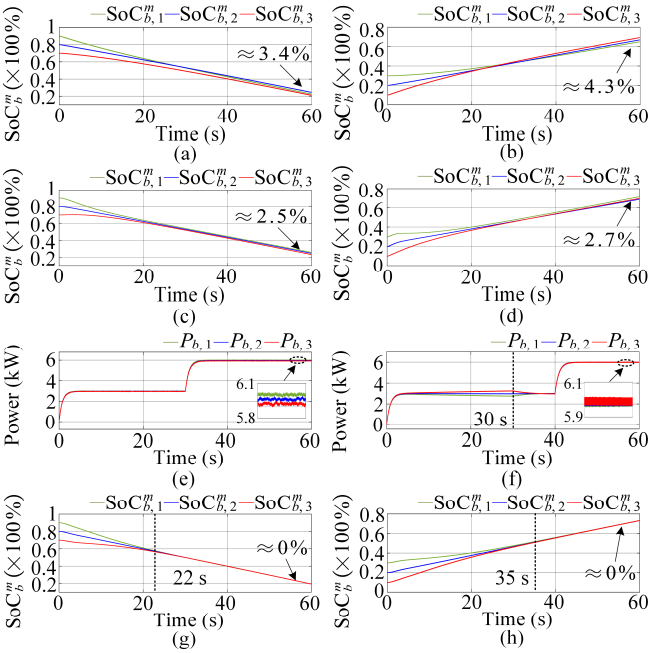

Fig. 7. Simulation results for case 2: (a) SoC balance in [17] in discharging mode, (b) SoC balance in [17] in charging mode, (c) SoC balance in [18] in discharging mode, (d) SoC balance in [18] in charging mode. (e) Power sharing in [18], (f) The performance of accurate power sharing control, (g) SoC balance in discharging mode, and (h) SoC balance in charging mode.

C. Case 3: HESS Operation

In this scenario, the batteries are operating within a limited range ($10\% \le \mathrm{SoC}_b^m \le 90\%$). From Fig. 8(a), PV and HESSs initially supply 10.5 kW to the loads that include dc and ac loads. At 10 s, a 3 kW load is added to the system. At 20 s, the microgrid is connected to the main grid. The main grid shares the 3 kW load. Subsequently, a 1 kW pulse load is installed in the system from 30 to 50 s. The frequency of the pulse load is set at 0.4 and 0.2 Hz during 30-40 s and 40-50 s, respectively. After 60 s, the dc load is removed, and then the HESSs absorb the excess power of the system. At 80 s, the microgrid is disconnected from the main grid and returned to islanded mode.

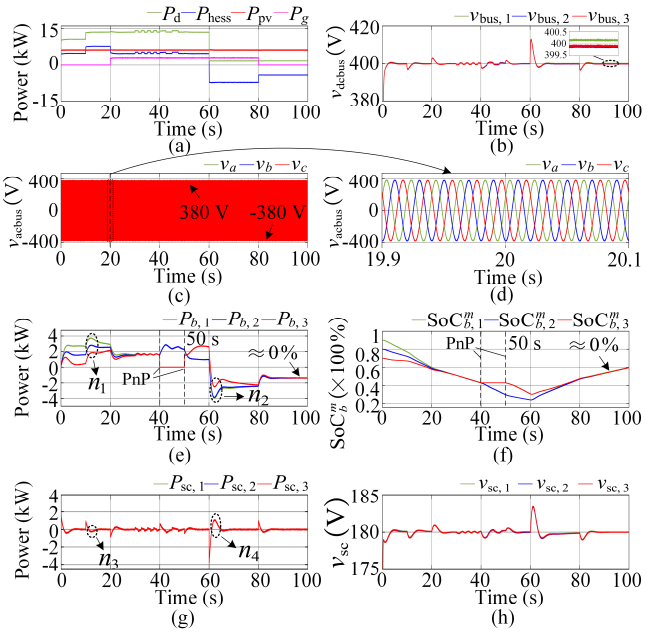

Fig. 8. Simulation results for case 3: (a) Power demand P_d, output power of the HESS, PV, and grid, (b) DC bus voltages, (c) AC bus voltage, (d) AC bus voltage between 19.9 s and 20.1 s, (e) Output power of batteries, (f) SoCs for batteries, (g) Output power of SCs, and (h) SoCs for SCs.

From Fig. 8(b), it can be seen that the bus voltages can be maintained within the set range even when the system power changes repeatedly. Besides, the difference among the three bus voltages is small. As can be seen in Figs. 8(c) and 8(d), when the microgrid is connected to the main grid, the ac bus voltage does not exhibit any oscillations.

From Figs. 8(e) and 8(f), the output power $P_{b,1}$ of b_1 is the highest due to the existence of SoC balancing control, while the output power $P_{b,3}$ of b_3 is the least. Therefore, the SoC gap among batteries is gradually reducing. In addition, b_3 is disconnected from the system at 40 s. This means that b_3 stops supplying power. Other batteries will automatically deliver more power to ensure system stability. At 50 s, b_3 is reconnected to the system and supplies power normally. From Fig. 8(g), the SCs only release/absorb power when the system power changes suddenly. At 10 s, a 3 kW load is connected to the system and the SCs provide power rapidly. Then, SCs receive a brief charge from the batteries [n_1 from Fig. 8(e) and n_3 from Fig. 8(g)]. At 60 s, the load is removed and the SCs absorb instantaneous power. Subsequently, the SCs briefly release power that is absorbed by the batteries [n_2 from Fig. 8(e) and n_4 from Fig. 8(g)]. Therefore, the SoCs of the SCs can be maintained at the reference value, the continuous use of SCs can be guaranteed, as shown in Fig. 8(h).

D. Case 4: SoC Limitation for Batteries

This case studies the batteries reaching the upper limit (90%) and lower limit (10%) of SoC. The initial states of the batteries' SoC are given in Table II.

From Figs. 9(a) and 9(c), the batteries are charged by the PV system. When the SoCs of the batteries reaches 90%, the proposed controller will automatically disconnect the battery to prevent overcharging. The power generated by PV will be greater than the load demand. Therefore, PV control will switch from MTTP mode to CVC mode to reduce output power at 32 s. At 34 s, all the batteries stop working. Then, an 11 kW load is installed in the system at 40 s. At this time, the total load of the system is greater than the power generated by the PV, hence the batteries will participate in providing power to the load. The SoC among the batteries is able to maintain balance throughout the operation. It should be noted that SCs are connected to the system during the entire operation to maintain the stability of the dc bus voltages, as shown in Figs. 9(b) and 9(d).

TABLE II
SOC LIMITATIONS FOR BATTERIES

Upper limits of SoC		Lower limits of SoC	
$SoC^m_{b,1}$	70 %	$SoC^m_{b,1}$	50 %
$SoC^m_{b,2}$	60 %	$SoC^m_{b,2}$	40 %
$SoC^m_{b,3}$	50 %	$SoC^m_{b,3}$	30 %

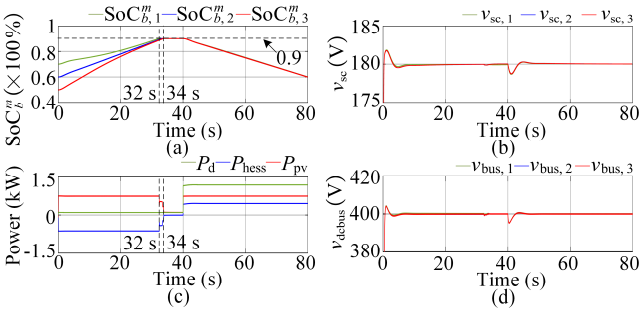

Fig. 9. Simulation results for case 4 ($SoC_b \geq 90\%$): (a) SoCs for batteries, (b) SoCs for SCs, (c) Power demand P_d, output power of the HESS and PV, and (d) DC bus voltages.

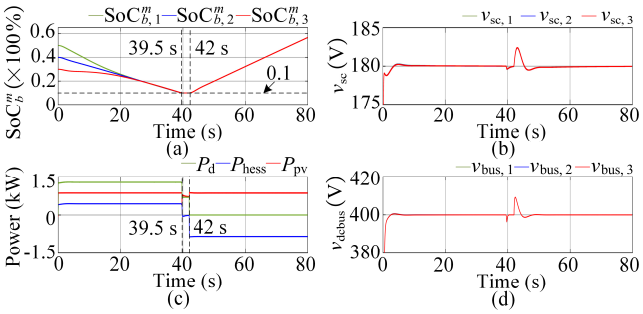

Fig. 10. Simulation results for case 4 ($SoC_b \leq 10\%$): (a) SoCs for batteries, (b) SoCs for SCs, (c) Power demand P_d, output power of the HESS and PV, and (d) DC bus voltages.

From Figs. 10(a) and 10(c), the batteries run in discharge mode. When the SoC of the batteries drops to 10% at 39.5 s, the batteries stop supplying power to the load. In addition, PV will switch to CVC mode, and the system load will be reduced appropriately. In addition, PV will switch to CVC mode, and the system load will be reduced appropriately. At 42 s, the system load was completely removed. The PV switches to MPPT mode to charge the batteries. During the entire operation process, SCs play a role in suppressing power fluctuations in the microgrid and ensuring that the bus voltages are within the safe range, as shown in Figs. 10(b) and Fig. 10(d).

VII. CONCLUSION

The novel coordinated droop controls are proposed in this paper. The *V*-d*P*/dt control is proposed to adjust the battery converter to deliver the low-frequency power, while the *V*-*P*

droop control is employed to regulate the SC converter to supply the high-frequency power. In addition, the bus voltage can be restored to the desired range through the SC control without an extra voltage recovery loop. The consensus-based voltage compensator is proposed to achieve the SoC balance among batteries and accurate power sharing. The proposed PMS can ensure that batteries operate within a safe range to prevent overuse. Then, the SoC of the SC can be automatically restored to the set value. In addition, the root locus method is employed to verify the stability of the proposed control system. Finally, the performance and feasibility of the proposed control method are verified by PIL simulation. The results of the simulation show that the proposed control works as expected.

REFERENCES

[1] R. Zamora and A. K. Srivastava, "Multi-layer architecture for voltage and frequency control in networked microgrid," *IEEE Trans. Smart Grid*, vol. 9, no. 3, pp. 2076-2085, May 2018.

[2] T. Dragicevic, X. N. Lu, J. C. Vasquez, and J. M. Guerrero, "DC microgrids-part I: a review of control strategies and stabilization techniques," *IEEE Trans. Power Electron.,* vol. 31, no. 7, pp. 4876-4891, Jul. 2016.

[3] T. Morstyn, B. Hredzak, and V. G. Agelidis, "Control strategies for microgrids with distributed energy storage systems: an overview," *IEEE Trans. Smart Grid,* vol. 9, no. 4, pp. 3652-3666, Jul. 2018.

[4] X. Qiu, T. A. Nguyen, and M. L. Crow, "Heterogeneous energy storage optimization for microgrids," *IEEE Trans. Smart Grid*, vol. 7, no. 3, pp. 1453–1461, May 2016.

[5] D. B. W. Abeywardana, B. Hredzak, V. G. Agelidis, and G. D. Demetriades, "Supercapacitor sizing method for energy-controlled filterbased hybrid energy storage systems," *IEEE Trans. Power Electron.*, vol. 32, no. 2, pp. 1626–1637, Feb. 2017.

[6] J. Shen and A. Khaligh, "A supervisory energy management control strategy in a battery/ultracapacitor hybrid energy storage system," *IEEE Trans. Transport. Electrific*., vol. 1, no. 3, pp. 223–231, Oct. 2015.

[7] Y. Gu, W. Li, and X. He, "Frequency-coordinating virtual impedance for autonomous power management of DC microgrid," *IEEE Trans. Power Electron.*, vol. 30, no. 4, pp. 2328–2337, Apr. 2015.

[8] S. K. Kollimalla, M. K. Mishra, A. Ukil, and H. B. Gooi, "DC grid voltage regulation using new HESS control strategy," *IEEE Trans. Sustain. Energy*, vol. 8, no. 2, pp. 772–781, Apr. 2017.

[9] U. Manandhar *et al*., "Energy management and control for grid connected hybrid energy storage system under different operating modes," *IEEE Trans. Smart Grid*, vol. 10, no. 2, pp. 1626-1636, Mar. 2019.

[10] X. Gao, and L. Fu, "SoC optimization based energy management strategy for hybrid energy storage system in vessel integrated power system", *IEEE Access*, vol. 8, pp. 54611–54619, Mar. 2020.

[11] Q. Zhang and G. Li, "Experimental study on a semi-active battery-supercapacitor hybrid energy storage system for electric vehicle application", *IEEE Trans. Power Electron*., vol. 35, no. 1, pp. 1014–1021, Jan. 2020.

[12] P. Lin, P. Wang, J. Xiao, J. Wang, C. Jin and Y. Tang, "An integral droop for transient power allocation and output impedance shaping of hybrid energy storage system in DC microgrid," *IEEE Trans. Power Electron*., vol. 33, no. 7, pp. 6262–6277, Jul. 2018.

[13] Q. Xu, J. Xiao, X. Hu, P. Wang, and M. Y. Lee, "A decentralized power management strategy for hybrid energy storage system with autonomous bus voltage restoration and state-of-charge recovery," *IEEE Trans. Ind. Electron.*, vol. 64, no. 9, pp. 7098–7108, Sep. 2017.

[14] T. Morstyn, B. Hredzak, and V. G. Agelidis, "Cooperative multi-agent control of heterogeneous storage devices distributed in a dc microgrid," *IEEE Trans. Power Syst*., vol. 36, no. 4, pp. 714–725, Jul. 2016.

[15] M. Shi, X. Chen, J. Zhou, Y. Chen, J. Wen, and H. He, "Advanced secondary voltage recovery control for multiple HESSs in a droop-controlled DC microgrid," *IEEE Trans. Smart Grid*, vol. 10, no. 4, pp. 3828-3839, July. 2019.

[16] P. Lin, T. Zhao, B. Wang, Y. Wang, and P. Wang, "A semi-consensus strategy toward multi-functional hybrid energy storage system in dc microgrids," *IEEE Trans. Energy Convers*., vol. 35, no. 1, Mar. 2020.

[17] R. Zhang, B. Hredzak, and T. Morstyn, "Distributed control with virtual capacitance for the voltage restorations, state of charge balancing and load allocations of heterogeneous energy storages in a DC datacenter microgrid," *IEEE Trans. Energy Convers*., vol. 34, no. 3, pp. 1296-1308, Sept. 2019.

[18] X. Lin, R. Zamora, and C. Baguley, "A coordinated droop controls and power management scheme for hybrid energy storage systems in DC microgrids," *in Proc. AUPEC*, Perth, Australia, 2021, pp.1-6.

[19] X. Lu, K. Sun, J. M. Guerrero, J. C. Vasquez, and L. Huang, "State-of-charge balance using adaptive droop control for distributed energy storage systems in DC microgrid applications," *IEEE Trans. Ind. Electron.,* vol. 61, no. 6, pp. 2804-2815, Jun. 2014.

[20] C. Li, E. A. A. Coelho, T. Dragicevic, J. M. Guerrero, and J. C. Vasquez, "Multiagent-based distributed state of charge balancing control for distributed energy storage units in AC microgrids," *IEEE Trans. Ind. Appl*., vol. 53, no. 3, pp. 2369–2381, May 2017.

[21] H.-J. Yoo, T.-T. Nguyen and H.-M. Kim, "Consensus-based distributed coordination control of hybrid AC/DC microgrids," *IEEE Trans. Sustain. Energy*, vol. 11, no. 2, pp. 629-639, Apr. 2020.

[22] M. Kriegleder, "A correction to algorithm A2 in 'asynchronous distributed averaging on communication networks," *IEEE/ACM Trans. Netw*., vol. 22, no. 6, pp. 2026–2027, Dec. 2014.

[23] L. Meng, T. Dragicevic, J. R. Perez, J. C. Vasquez and J. M. Guerrero, "Modeling and sensitivity study of consensus algorithm-based distributed hierarchical control for DC microgrids," *IEEE Trans. Smart Grid*., vol. 7, no. 5, pp. 1504-1515, May 2016.

[24] R. Olfati-Saber, J. Fax, and R. Murray, "Consensus and cooperation in networked multi-agent systems," *Proceedings of the IEEE*, vol. 95, no. 1, pp. 215–233, 2007.

[25] Z. Fan, K. Thanapalan, A. Procter, S. Carr, and J. Maddy, "Adaptive hybrid maximum power point tracking method for a photovoltaic system," *IEEE Trans. Energy Convers*., vol. 28, no. 2, pp. 353–360, Apr. 2013.

Xin Lin received the B.S. in electrical engineering from Waikato Institute of Technology, Hamilton, New Zealand, in 2016, and M.S. degree in electrical engineering from Auckland University of Technology, Auckland, New Zealand, in 2017. He is currently a Ph.D. candidate in electrical engineering at Auckland University of Technology, Auckland, New Zealand.

His current research interests include microgrids, intelligent energy management system, and power converter control.

Ramon Zamora received the Ph.D. degree in electrical engineering from Washington State University, Pullman, WA, USA, in 2015. He is a Lecturer with the Auckland University of Technology. His research interests include power system modeling, simulation and control, power system management and controls, power electronic application for power systems, grid integration of renewable energy and energy storage, microgrid and smart grid, and distributed controls.

Craig A. Baguley (M'11) received the Ph.D. degree from the University of Auckland, Auckland, New Zealand, in 2011. He is currently with the Auckland University of Technology, Auckland. His research interests include high-voltage pulse transformer design, high frequency induction heating, electrical muscle stimulation techniques, and high current power supply design.